

**Electronic Supplementary Information for
“Determining role of structural flexibility on
catalytic activity of conductive 2D layered
metal–organic frameworks”**

Mohammad R. Momeni*, Zeyu Zhang, and Farnaz A. Shakib*

*Department of Chemistry and Environmental Science, New Jersey Institute of Technology,
Newark 07102, NJ United States*

E-mail: momeni@njit.edu, shakib@njit.edu

Contents

S1. Theoretical approach	3
S2. Force field development for the $\text{Co}_3(\text{HTTP})_2$ MOF	4
Figure S1	5
Table S1	6
Table S2	7
Table S3	8
Table S4	9
Table S5	10
S3. Validation of the developed force field	11
Figure S2	11
Figure S3	12
Figure S4	12
Figure S5	14
S4. Electronic structure calculations	15
S5. MD simulation details	16
S6. Catalytic activity of different Co sites in ODH of propane	17
Figure S7	18
Figure S8	19
Table S6	20
Table S7	21

S1. Theoretical approach

Accurate determination of realistic molecular models for flexible materials such as 2D π -stacked layered $\text{Co}_3(\text{HTTP})_2$ MOF has many implications to their chemical stability and reactivity in both gas phase and aqueous solutions. However, conventional *static* electronic structure calculations reported in the literature neglect temperature and solvent effects and assume a *close to perfect* structure for the material under study with no deformations/defects and/or grain boundaries. A prominent example is the theoretical studies performed on the 2D conductive $\text{Ni}_3(\text{HITP})_2$ MOF. While $\text{Ni}_3(\text{HITP})_2$ was synthesized as a semiconductor,¹ the following theoretical studies unanimously reported a metallic band gap for this layered MOF.²⁻⁴ A very recent density functional theory (DFT) study, however, has suggested that including defects can break the π -conjugation and decrease the dispersion of the electronic bands near the Fermi level and hence bring the calculated band gaps closer to the experimentally measured semiconducting values.³ Our multi-faceted dynamical approach used in this work allows deformation of the π -stacked layers which leads to the weakening of through-space π -conjugation and slipping of layers compared to each other, painting a realistic picture of the layered architecture of 2D MOFs. In this approach, we first screened $\text{M}_3(\text{H}(\text{H},\text{I},\text{T})\text{TP})_2$ MOFs using electronic structure calculations and determined that 2D $\text{Co}_3(\text{HTTP})_2$ has the highest reactivity toward C-H activation of propane to propene and hence we chose it as the representative of the 2D MOFs to be studied in this work. Then, starting from the experimentally reported crystal structure of $\text{Co}_3(\text{HHTP})_2$,⁵ where HHTP=2,3,6,7,10,11-hexahydroxytriphenylene, a crystal structure comprised of two layers and a total of 126 atoms was built for the 2D $\text{Co}_3(\text{HTTP})_2$ MOF. Next, an extended $2 \times 2 \times 2$ supercell comprised of four layers with 48 open Co sites and a total of 1008 atoms was built from the original unit cell and optimized via dispersion corrected periodic DFT calculations. The metal nodes of the optimized crystal structure then served as the starting point for developing our *ab initio* force field which opposite to prohibitively expensive *ab initio* molecular dynamics simulations allowed for long-time simulation of the dynamics of

$2 \times 2 \times 2$ supercell with and without water as solvent.

S2. Force field development for the $\text{Co}_3(\text{HTTP})_2$ MOF

To parametrize our force field for the $\text{Co}_3(\text{HTTP})_2$ MOF framework, the David Carrol’s genetic algorithm⁶ was used for fitting all the interactions involving the Co^{2+} transition metal center including all bonds, angles, and dihedrals while the rest of the parameters involving the organic linkers were taken from the generalized amber force field (GAFF)⁷ without further modification. To generate our training set, a reduced cluster model comprised of a single Co center and two dithiophenolate linkers, see Figure S1, was cut from the PBE-D3 optimized crystal structure. Potential energy scans were performed for fitting the parameters involving Co. To this end, a training set was built from this cluster by displacing the central Co atom by 0.02 Å from -0.04 Å to +0.04 Å along the x , y and z dimensions. All electronic energies for these clusters were then computed using the highly accurate $\omega\text{B97M-v}$ ⁸ density functional and the def2-TZVP basis set as implemented in QCHEM 5.2.⁹ Morse potential was used for all coordinative Co-S bonds while harmonic potential was employed for the rest. Atomic charges were computed at the M06-2X/def2-TZVP level using the CHELPG scheme which fits all atomic charges to represent molecular electrostatic potential.¹⁰ The complete list of the force field parameters for $\text{Co}_3(\text{HTTP})_2$ MOF is given in Tables S1-S5 below.

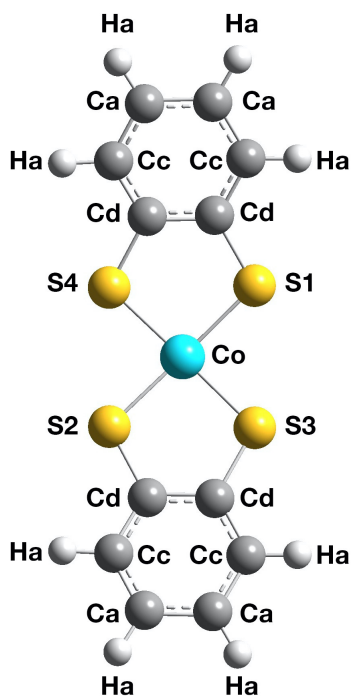


Figure S1: Molecular model and the atom labels used in developing the *ab initio* force field for the 2D Co₃(HTTP)₂ MOF.

Table S1: Electrostatic and Lennard-Jones non-bonded parameters for $\text{Co}_3(\text{HTTP})_2$ MOF where r_{ij} refers to the distance between two atoms.

$$V_{LJ}(r) = 4\epsilon \left[\left(\frac{\sigma}{r_{ij}} \right)^{12} - \left(\frac{\sigma}{r_{ij}} \right)^6 \right] \quad (1)$$

Atom name	Atom type	Charge	ϵ (kcal·mol ⁻¹)	$\sigma/2$ (Å)
Co	Co	0.9277	0.0015	1.0840
S1	S1	-0.3801	0.2500	1.7818
S2	S2	-0.3831	0.2500	1.7818
S3	S3	-0.3463	0.2500	1.7818
S4	S4	-0.3543	0.2500	1.7818
Ca	C	-0.0282	0.0860	1.6998
Cd	C	0.0443	0.0860	1.6998
Cc	C	-0.0032	0.0860	1.6998
Ha	H	0.1211	0.0150	1.2998

Table S2: Morse bond potential parameters for $\text{Co}_3(\text{HTTP})_2$ MOF.

$$V_{Morse}(r) = E_0[(1 - e^{-K_{ij}(r_{ij}-r_0)})^2 - 1] \quad (2)$$

Bonds	E_0 (kcal·mol ⁻¹)	r_0 (Å)	K_{ij} (Å ⁻¹)
Co-S1	27.5769	2.1485	1.7464
Co-S2	28.9104	2.1186	0.5122
Co-S3	44.5717	2.1271	1.1696
Co-S4	55.5368	2.1551	0.8290

Table S3: Harmonic bond potential parameters for $\text{Co}_3(\text{HTTP})_2$ MOF.

$$V_{bond}(r) = \frac{1}{2}K_{ij}(r_{ij} - r_0)^2 \quad (3)$$

Bonds	K_{ij} (kcal·mol ⁻¹ ·Å ⁻²)	r_0 (Å)
Cd-S1	531.6000	1.7560
Cd-S2	531.6000	1.7560
Cd-S3	531.6000	1.7560
Cd-S4	531.6000	1.7560
Ca-Cc	770.2000	1.4560
Ca-Ca	922.2000	1.3980
Ca-Ha	691.6000	1.0860
Cc-Ha	698.2000	1.0840
Cc-Cd	1001.8000	1.3730
Cd-Cd	839.6000	1.4280

Table S4: Bending potential parameters for $\text{Co}_3(\text{HTTP})_2$ MOF.

$$V_{\text{angle}}(\theta) = \frac{1}{2}K_{ijk}(\theta_{ijk} - \theta_0)^2 \quad (4)$$

Angles	K_{ijk} (kcal·mol ⁻¹ ·deg ⁻²)	θ (°)
S1-Co-S2	115.256992	174.264971
S1-Co-S3	296.962735	82.479565
S1-Co-S4	175.969673	86.358363
Co-S1-Cd	250.077391	100.034838
Co-S2-Cd	75.006080	100.655413
Co-S3-Cd	176.240040	106.889207
Co-S4-Cd	124.560189	101.692449
S2-Co-S3	210.520278	87.442248
S2-Co-S4	62.294256	89.059319
S3-Co-S4	5.348401	166.559529
Cd-Cd-S1	123.800003	120.199997
Cd-Cd-S2	123.800003	120.199997
Cd-Cd-S3	123.800003	120.199997
Cd-Cd-S4	123.800003	120.199997
Cc-Cd-S1	129.600006	111.500000
Cc-Cd-S2	129.600006	111.500000
Cc-Cd-S3	129.600006	111.500000
Cc-Cd-S4	129.600006	111.500000
Ca-Cc-Ha	91.599998	124.000000
Ca-Cc-Cd	135.199997	113.500000
Ca-Ca-Cc	130.000000	120.699997
Ca-Ca-Ha	96.400002	119.800003
Cc-Ca-Ha	96.400002	119.800003
Cc-Cd-Cd	136.399994	114.099998
Cd-Cc-Ha	97.000000	121.699997

Table S5: Torsion potential parameters for $\text{Co}_3(\text{HTTP})_2$ MOF.

$$V_{\text{torsion}}(\phi) = K_{ijkl}[1 + \cos(m\phi_{ijkl} - \delta)] \quad (5)$$

Dihedrals	K_{ijkl} (kcal·mol ⁻¹)	δ (°)	m
S1-Co-S2-Cd	0.260628	180.0000	1
S1-Co-S3-Cd	0.734261	180.0000	1
S1-Co-S4-Cd	7.133819	180.0000	1
Cc-Cd-S2-Co	2.297983	180.0000	1
S3-Co-S2-Cd	1.457406	180.0000	1
S4-Co-S2-Cd	0.843209	180.0000	1
Cd-Cd-S3-Co	0.039513	180.0000	1
S2-Co-S1-Cd	0.029411	180.0000	1
S3-Co-S1-Cd	3.703464	180.0000	1
S4-Co-S1-Cd	4.084026	180.0000	1
Cd-Cd-S4-Co	5.522001	180.0000	1
S2-Co-S3-Cd	1.282251	180.0000	1
S2-Co-S4-Cd	6.249624	180.0000	1
Cc-Cd-S3-Co	6.593489	180.0000	1
S3-Co-S4-Cd	0.141205	180.0000	1
Cc-Cd-S4-Co	2.085528	180.0000	1
Cd-Cd-S1-Co	0.405533	180.0000	1
Cd-Cd-S2-Co	1.268701	180.0000	1
S4-Co-S3-Cd	0.062286	180.0000	1
Cc-Cd-S1-Co	0.218071	180.0000	1
Ca-Cc-Cd-S2	12.0000	180.0000	2
Ca-Cc-Cd-Cd	12.0000	180.0000	2
Ca-Ca-Cc-Ha	5.6000	180.0000	2
Ca-Ca-Cc-Cd	5.6000	180.0000	2
Cc-Cd-Cd-S1	12.0000	180.0000	2
S1-Cd-Cd-S4	12.0000	180.0000	2
Ca-Cc-Cd-S1	12.0000	180.0000	2
Ha-Cc-Cd-S1	12.0000	180.0000	2
Cc-Ca-Ca-Cc	9.0000	180.0000	2
Cc-Ca-Ca-Ha	9.0000	180.0000	2
Cc-Cd-Cd-Cc	12.0000	180.0000	2
Cc-Cd-Cd-S3	12.0000	180.0000	2
Ha-Ca-Cc-Ha	5.6000	180.0000	2
Ha-Cc-Cd-S2	12.0000	180.0000	2
Ha-Cc-Cd-Cd	12.0000	180.0000	2
Ha-Ca-Cc-Cd	5.6000	180.0000	2
Cc-Cd-Cd-S2	12.0000	180.0000	2
S2-Cd-Cd-S3	12.0000	180.0000	2
Ca-Cc-Cd-S3	12.0000	180.0000	2
Ha-Cc-Cd-S3	12.0000	180.0000	2
Ca-Cc-Cd-S4	12.0000	180.0000	2
Ha-Cc-Cd-S4	12.0000	180.0000	2
Cc-Cd-Cd-S4	12.0000	180.0000	2
Ha-Ca-Ca-Ha	9.0000	180.0000	2

S3. Validation of the developed force field

We validated our developed force field for $\text{Co}_3(\text{HTTP})_2$ against available experimental data. The interlayer distances obtained from our MD simulations are compared to the experimentally measured powder X-ray diffraction data as shown in Figure S2a below. We have used Bragg's equation ($\lambda = 2d\sin(\theta)$) to calculate the interlayer distance from the broad peak at $2\theta = 7.2^\circ$ resulting in $d = 3.3 \text{ \AA}$. The calculated radial distribution functions (RDFs) of Co-Co distances in dry $\text{Co}_3(\text{HTTP})_2$, black line in Figure S2b, shows a prominent broad peak centered $\sim 4.2 \text{ \AA}$ which indicates constant breathing of the stacked layers in the z direction. Deformation of flexible linkers leads to local instances of the increase of interlayer distances which would return to a shorter value afterward, creating the breathing movement. Consequently, the equilibrated dry framework shows interlayer distances as small as $\approx 3.3 \text{ \AA}$, in agreement with the interlayer distance found from PXRD results below.¹¹

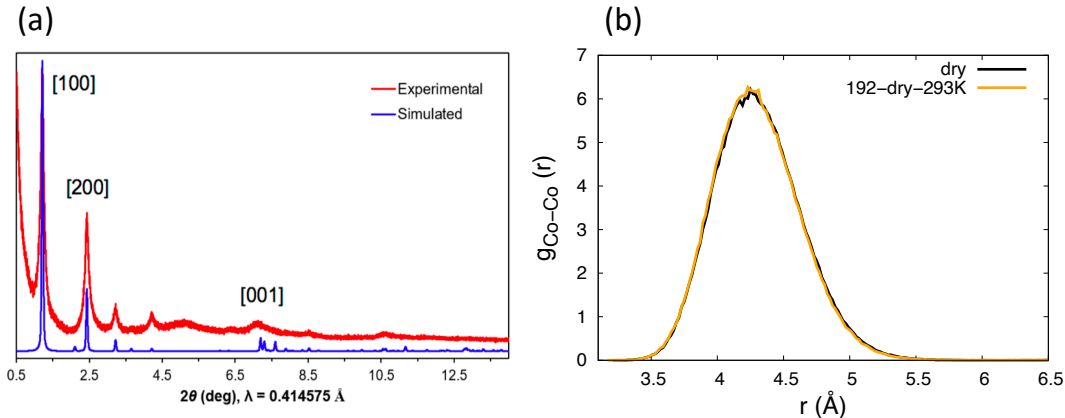


Figure S2: (a) Experimental and simulated PXRD patterns of $\text{Co}_3(\text{HTTP})_2$, adapted with permission from Ref 11 copyright (2017) American Chemical Society. (b) Calculated RDFs of the Co-Co interlayer distances in dry, in black, as well as water-removed, in yellow, frameworks at 293 K.

Figure S3 illustrates the distribution of all 4 types of metal-thio bond lengths in dry and water-contained $2 \times 2 \times 2$ $\text{Co}_3(\text{HTTP})_2$ systems where all show a prominent peak around the *ab initio* reference bond length of $\approx 2.15 \text{ \AA}$.

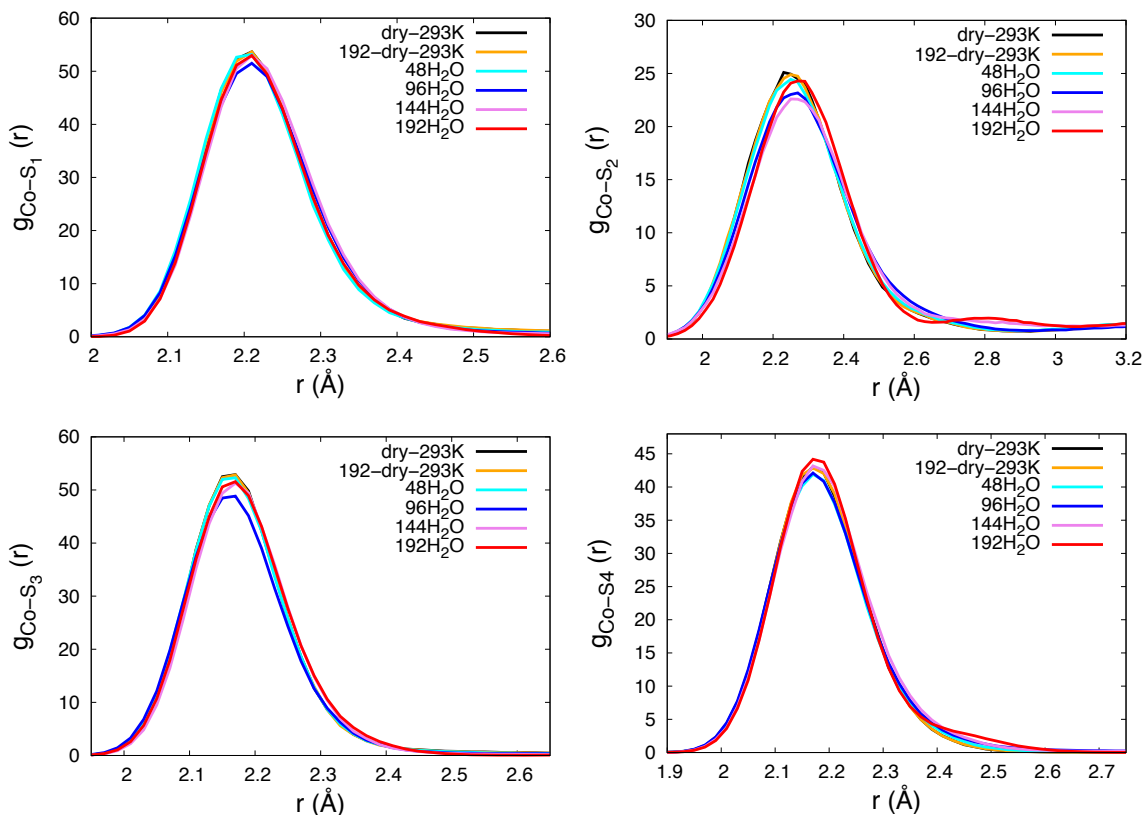


Figure S3: Calculated RDFs of all Co-S_x ($x = 1 - 4$) bonds in dry as well as hydrated $\text{Co}_3(\text{HTTP})_2$ MOFs with different relative humidities at 293 K.

Further validation of the developed force field for $\text{Co}_3(\text{HTTP})_2$ MOF comes from our potential energy surface scans of the metal-thio bonds, Figure S4. As can be seen, the difference between the calculated results using our developed force field and the reference $\omega\text{B97M-v}$ method is small especially around the minimum Co-S bond distance of ≈ 2.15 Å for both doublet and quartet spin states.

Finally, to validate the dynamical motions observed with our developed force field, we compared the results of our classical MD simulations to the *ab initio* molecular dynamics (AIMD) simulation data in the NVT ensemble. Given the known prohibitively expensive nature of the on-the-fly AIMD we performed these simulations on the $1 \times 1 \times 1$ $\text{Co}_3(\text{HTTP})_2$ crystal structure and up to 7 ps and compared the final equilibrated systems to the 0 K optimized structure keeping the methodology and setting the same as outlined in the main

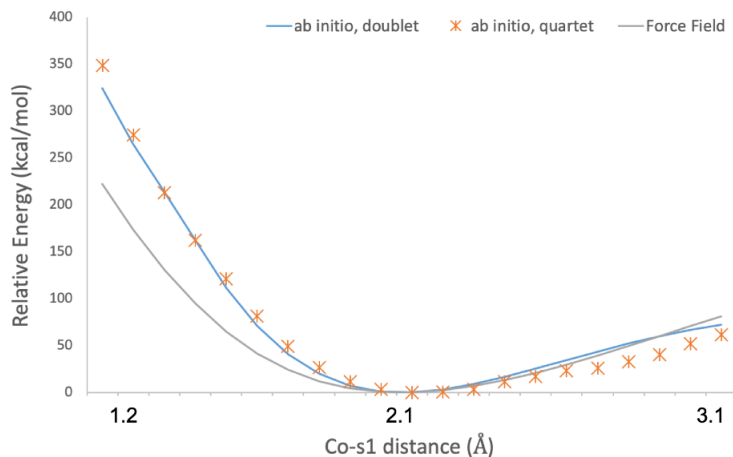


Figure S4: Comparison of our force field and reference *ab initio* energies at the ω B97M-v/def2-TZVP level for both the doublet and quartet spin states of the Co^{2+} cluster model shown in Figure S1. To obtain these correlation plots, the Co-s1 bond is scanned from 1.15 Å to 3.15 Å with the minimum bond distance occurring at ≈ 2.15 Å.

text. The resulted structures are shown in Figure S5 where one can clearly detects slipping, rippling and breathing of layers in this short simulation time. It worth mentioning that these AIMD results are provided only to give a glimpse into the dynamical nature of the 2D MOFs. Ideally, these AIMD simulations need to be run in the NPT ensemble that allows the change of volume of unit cell to accommodate the dynamical breathing motions of the layers. As mentioned, capturing the flexibility of layers necessitate a very long simulation time, in the orders of hundreds of ps, in order to reach an equilibrium state. Even if that goal were achieved, the result still wouldn't be good enough considering the small size of this crystal that can not represent real dynamics of the system. This is another reason for the importance of the developed AIFF in this work that renders nanosecond simulations feasible on unit cells with 10 times more atoms.

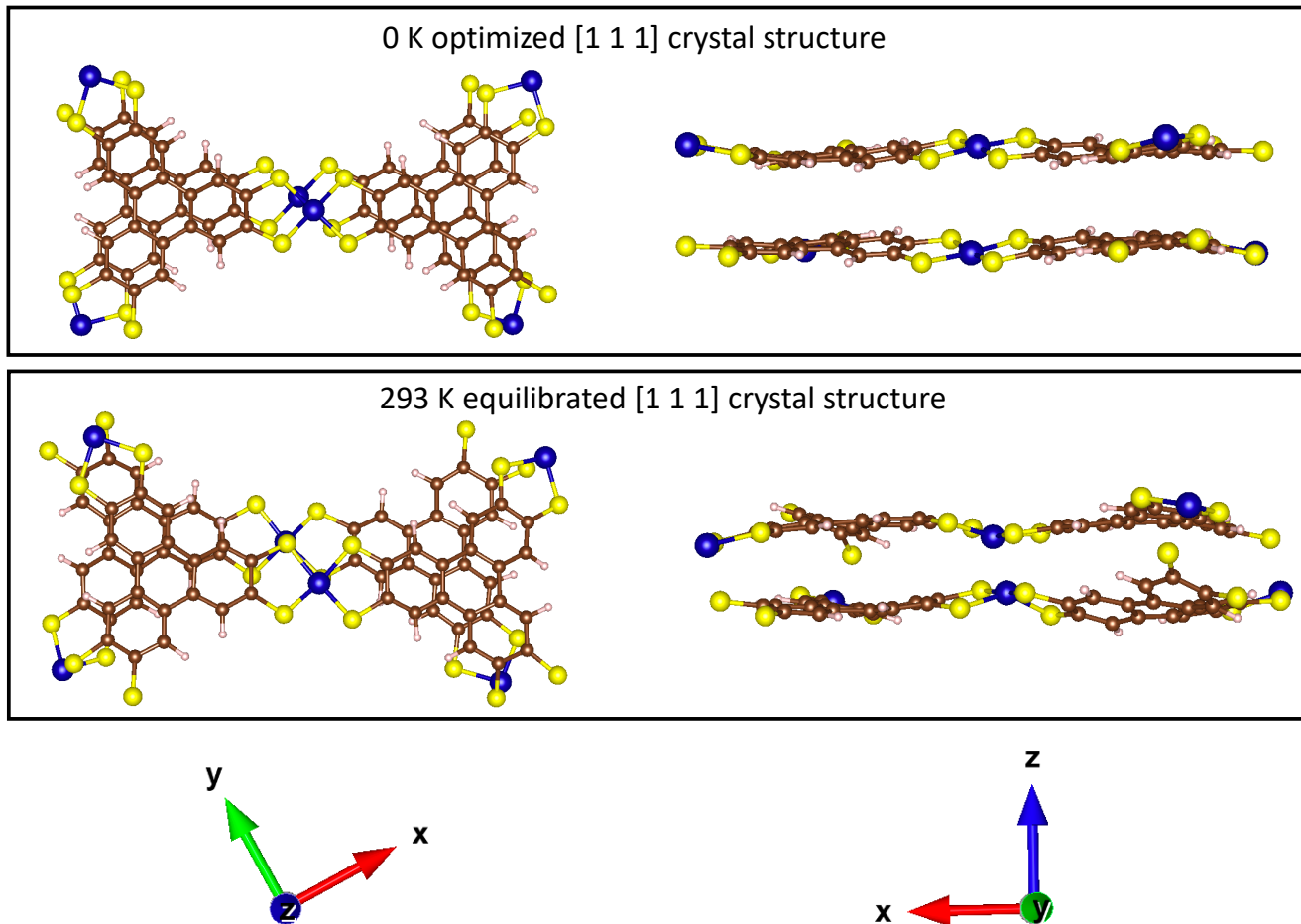


Figure S5: Comparison of the PBE-D3(BJ) 0 K optimized (top) and 293 K AIMD equilibrated (bottom) $1 \times 1 \times 1$ $\text{Co}_3(\text{HTTP})_2$ systems with using the periodic boundary condition. Slipping movement in ab plane is evident from the bottom left image while deformation of organic linkers and increase and decrease of the interlayer distance is evident from the bottom right figure. The latter creates rippling layers and a constant breathing motion alongside the c vector. In this Figure colors blue, yellow, brown and pink represent Co, S, C, and H, respectively.

S4. Electronic structure calculations

Periodic Calculations.

In our periodic electronic structure calculations, the PBE-D3(BJ) density functional in conjunction with the double-zeta valence with polarization DZVP-MOLOPT basis sets and core-electron pseudo potentials according to the Geodecker-Teter-Hutter formulation¹² as implemented in CP2K were employed. The plane-wave cutoff of the finest grid and REL_CUTOFF were set to 500 RY and 60 RY. MAX_FORCE (hartree/bohr), RMS_FORCE, MAX_DR (bohr), and RMS_DR were set to 0.0030, 0.0050, 0.0020 and 0.0050, respectively.

Cluster calculations.

Cluster models were cut from the PBE-D3(BJ)/DZVP-MOLOPT optimized periodic unit cells of the different $M_3(\text{HHTP})_2$ and $M_3(\text{HTTP})_2$ ($M = \text{Co}$ and Cu) MOFs. To obtain these cluster models, the organic linkers around the single-metal node were truncated to dithiophenolates and catecholates groups with the two linking carbon atoms saturated with hydrogen atoms fixed to mimic the rigidity of the framework. Geometries were then minimized in the gas phase using the M06-L meta-GGA exchange-correlation density functional.^{13,14} The def2-SVP^{15,16} basis set was used for all elements. All basis sets were obtained from the basis set exchange database.¹⁷ The default “ultrafine” grid used for numerical integrations in DFT, i.e., a pruned grid of 99 radial shells and 590 angular points per shell. The natures of all stationary points were determined by calculation of analytic vibrational frequencies, which were also used to compute molecular partition functions (298 K, 1 atm) using the conventional particle-in-a-box, rigid-rotator, quantum mechanical harmonic oscillator approximation,¹⁸ except that all vibrational frequencies below 50 cm^{-1} were replaced with values of 50 cm^{-1} (the quasi-harmonic-oscillator approximation).¹⁸ Zero-point vibrational energies and thermal contributions to enthalpy were determined from these partition functions. For transition-state structures, the presence of a single imaginary frequency corresponding to the

reaction path of interest was confirmed. IRC calculations further confirmed the nature of these stationary states. Electronic energies were further refined by performing single point calculations with the M06-2X^{14,19} meta-GGA hybrid density functional on gas phase optimized geometries with the larger def2-TZVP^{15,16} basis set. Default convergence criteria for geometry optimizations and single point energy calculations were used. All reported cluster free energies and enthalpies in the text and here are computed by combining M06-2X single point energies with thermochemical contributions obtained at the M06-L(gas phase) level. All cluster computations for mechanistic studies were carried out with Gaussian16.²⁰

S5. MD simulation details

All classical MD simulations were started from the hexagonal ($\alpha = \beta = 90^\circ$, $\gamma = 120^\circ$, $a = b = 46.470 \text{ \AA}$, and $c = 13.555 \text{ \AA}$) PBE-D3 minimized tetra-layered $2 \times 2 \times 2$ supercell of the bulk $\text{Co}_3(\text{HTTP})_2$ MOF (with 48 open Co sites and 1008 atoms in total) using DL_POLY_2.²¹ The dry system was simulated at temperatures ranging from 93 K – 393 K. All systems were equilibrated for 5 ns in five 1 ns consecutive isothermal-isobaric (NPT) and constant-temperature constant-stress ($N\sigma T$) ensembles with a time step of 0.2 fs. The equations of motion were propagated according to the velocity-Verlet algorithm. The temperature was kept constant using a Nosé-Hoover chain comprised of four thermostats.²² An atom-atom distance of 6.0 \AA was employed for truncating the short-range interactions and the electrostatics were calculated using the Ewald summation method.²³ To account for errors due to the truncation at 6.0 \AA , long-range electrostatic interactions as implemented in DL_POLY_2 were applied to Lennard-Jones potentials.²¹ Lorentz-Berthelot mixing rules were used to drive cross interaction terms.

S6. Catalytic activity of different Co sites in ODH of propane

The proposed mechanism by Barona *et al.*²⁴ for oxidative dehydrogenation of propane using N_2O as oxidizing agent (Figure 3) is adopted for studying the effects of temperature and solvent triggered heterogeneity and structural deformations on catalytic activity of $\text{Co}_3(\text{HTTP})_2$ via coordinatively unsaturated Co sites. This mechanism is comprised of the following elementary steps: (step 1) binding of the N_2O oxidizing agent to the open metal site followed by metal-oxo bond formation and N_2 liberation; (step 2) C–H bond activation of the secondary hydrogen of propane; (step 3) propyl radical rebound to the metal-hydroxyl group to form propanol or another C–H activation to form terminal water and propene and (step 4) water/propanol desorption to complete the catalytic cycle and regenerate the catalytic open metal site. To ease the burden of catalytic computations, we relaxed only the positions of the oxygen and the attached Co sites while the rest of the framework kept fixed at their equilibrated positions, Figure S6 . To confirm the validity of this approach we tested a variety of models by expanding the segments of the framework to be relaxed. In the largest such model, we relaxed the top and bottom layers located in one segment, Figure S6. As can be seen on the Figure, the difference in energy is only +0.2 kcal/mol confirming the validity of the smaller model for our calculations.

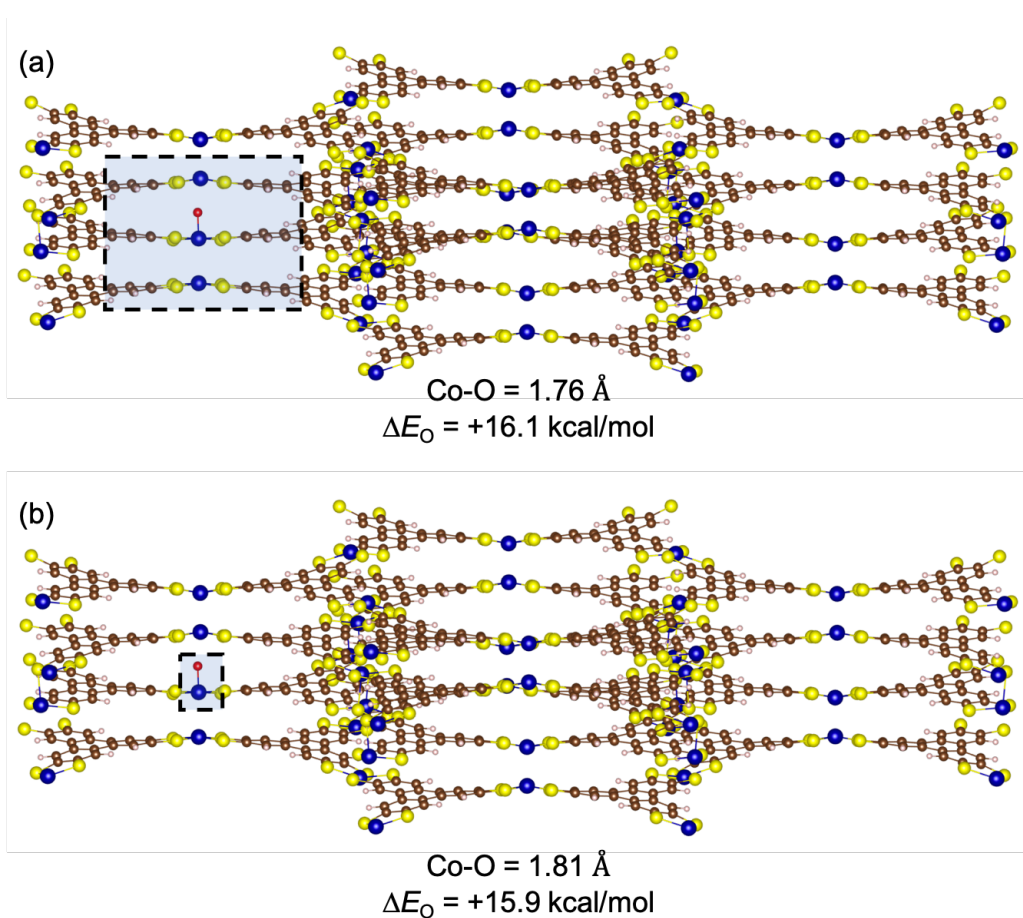


Figure S6: Two different models tested for studying the catalytic activity of different Co sites of $\text{Co}_3(\text{HTTP})_2$ in ODH of propane with the relaxed segments highlighted with dashed boxes. The Co-O bond distances (in Å) and oxygen bond formation energies calculated at the PBE-D3/DZVP-MOLOPT level are given for each model.

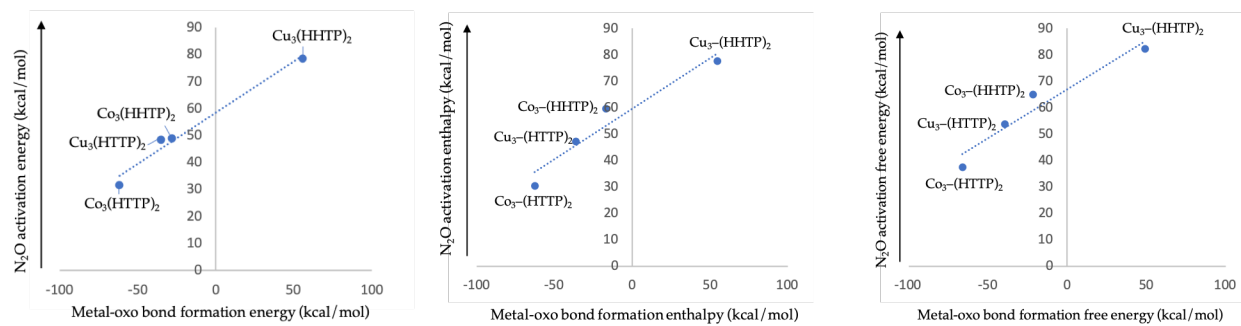


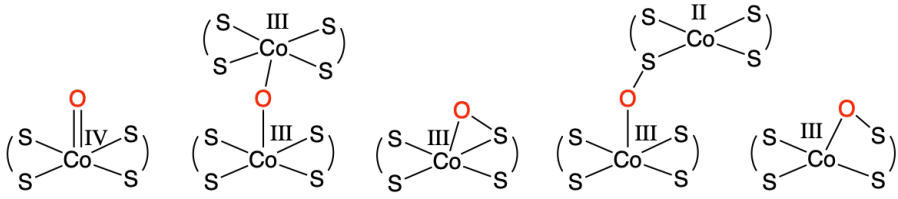
Figure S7: Plot of the N₂O activation energy, enthalpy and free energy barriers against their corresponding M-oxo bond formation energies (M = Co and Cu). Linear regression lines $y = 0.3812x + 58.449$ and $R^2 = 0.98$ for electronic energies, $y = 0.3835x + 59.548$, $R^2 = 0.93$ for enthalpies and $y = 0.3709x + 66.714$, $R^2 = 0.93$ for free energies.

Table S6: PBE-D3/DZVP-MOLOPT computed metal-oxo bond formation energies (ΔE_{M-O} in kcal/mol) and RESP charges on all 48 Co sites of the empty 2D bulk $\text{Co}_3(\text{HTTP})_2$ 0K@MOF system. The computed average values of ΔE_{M-O} and RESP charges for all different isomers are also given. In the adopted nomenclature, numbers refer to the atom label of the Co centers in the considered $2 \times 2 \times 2$ supercell.

Systems	ΔE_{M-O}	RESP charges	Systems	ΔE_{M-O}	RESP charges
Co-121	+0.5	+0.398	Co-625	-25.7	+0.391
Co-122	+16.3	+0.354	Co-626	+16.8	+0.355
Co-123	-25.8	+0.393	Co-627	-25.4	+0.391
Co-124	+0.7	+0.400	Co-628	-32.0	+0.393
Co-125	-13.9	+0.357	Co-629	+14.0	+0.355
Co-126	-22.0	+0.391	Co-630	-34.9	+0.390
Co-247	+1.8	+0.388	Co-751	-35.1	+0.391
Co-248	-13.0	+0.353	Co-752	-13.9	+0.353
Co-249	-25.5	+0.397	Co-753	-25.5	+0.396
Co-250	+0.8	+0.391	Co-754	+0.1	+0.388
Co-251	+15.8	+0.362	Co-755	+18.1	+0.354
Co-252	-35.3	+0.395	Co-756	-31.3	+0.393
Co-373	-25.3	+0.397	Co-877	-31.7	+0.388
Co-374	+15.9	+0.348	Co-878	+15.9	+0.350
Co-375	+0.7	+0.398	Co-879	-34.9	+0.398
Co-376	-32.4	+0.388	Co-880	-22.0	+0.391
Co-377	-13.8	+0.355	Co-881	-13.9	+0.354
Co-378	-34.9	+0.392	Co-882	+1.0	+0.392
Co-499	+5.9	+0.392	Co-1003	-35.0	+0.395
Co-500	-14.0	+0.355	Co-1004	+15.7	+0.353
Co-501	+0.8	+0.393	Co-1005	-35.0	+0.389
Co-502	+0.8	+0.397	Co-1006	+2.2	+0.401
Co-503	+16.2	+0.355	Co-1007	+16.2	+0.355
Co-504	+0.8	+0.392	Co-1008	+1.3	+0.391
Avg (Co)			Avg (S)		
Avg (Co-Co (int))			Avg (S)		
Avg (Co-S)			Avg (S)		
Avg (S)			Avg (S)		
Avg (ALL) ^(a)			Avg (S)		

(a) S isomers are excluded as the off-cycle species.

Table S7: PBE-D3/DZVP-MOLOPT computed metal-oxo bond formation energies (ΔE_{M-O} in kcal/mol) and RESP charges on all 48 Co sites of the 293 K MD equilibrated 293_dry@MOF system. The computed average values of ΔE_{M-O} and RESP charges for all different isomers are also given for comparison. In the adopted nomenclature, numbers refer to the atom label of the Co centers in the considered $2 \times 2 \times 2$ supercell.



The figure shows five chemical structures representing different Co environments in a MOF system. Each structure consists of a central Co atom (labeled with Roman numerals I, II, III, or IV) coordinated to four S atoms in a tetrahedral-like arrangement. In the 'Co-S' and 'Co-S (d)' structures, an additional O atom is coordinated to the Co atom, forming a metal-oxo bond. The O atom is shown in red. The 'Co-S (int)' structure shows the O atom bridging between two Co atoms.

“Co”			“Co-Co (int)”			“Co-S”			“Co-S (int)”			“Co-S (d)”		
Systems	ΔE_{M-O}	RESP charges	Systems	ΔE_{M-O}	RESP charges	Systems	ΔE_{M-O}	RESP charges	Systems	ΔE_{M-O}	RESP charges	Systems	ΔE_{M-O}	RESP charges
Co-31	-44.1	+0.201	Co-537	-10.1	+0.383									
Co-32	-34.9	+0.322	Co-538	-24.9	+0.310									
Co-63	-14.5	+0.244	Co-573	-29.7	+0.318									
Co-64	-43.7	+0.398	Co-574	-26.9	+0.480									
Co-75	-34.5	+0.311	Co-588	-16.8	+0.362									
Co-126	-18.7	+0.264	Co-636	-17.0	+0.272									
Co-127	-19.1	+0.229	Co-637	-26.7	+0.274									
Co-138	-19.9	+0.242	Co-651	-19.8	+0.286									
Co-189	-7.6	+0.256	Co-699	-38.5	+0.235									
Co-190	-45.8	+0.583	Co-700	-45.7	+0.453									
Co-191	-32.2	+0.318	Co-712	-37.6	+0.241									
Co-222	-41.9	+0.259	Co-739	-15.6	+0.326									
Co-283	-43.0	+0.303	Co-789	-26.6	+0.281									
Co-284	-44.5	+0.305	Co-790	-24.9	+0.287									
Co-315	-20.5	+0.287	Co-825	-28.7	+0.316									
Co-316	-30.6	+0.421	Co-826	-39.2	+0.483									
Co-327	-27.8	+0.339	Co-840	-31.0	+0.314									
Co-378	-34.0	+0.208	Co-888	-4.2	+0.178									
Co-379	-28.3	+0.300	Co-889	-27.3	+0.345									
Co-390	-21.0	+0.222	Co-903	-22.9	+0.243									
Co-441	-37.9	+0.272	Co-951	-37.9	+0.326									
Co-442	-63.9	+0.489	Co-952	-44.5	+0.433									
Co-443	-39.6	+0.307	Co-964	-31.8	+0.209									
Co-474	-12.4	+0.277	Co-991	-36.3	+0.276									
Avg (Co)	-13.0	+0.239												
Avg (Co-Co (int))	-21.0	+0.222												
Avg (Co-S)	-25.6	+0.293												
Avg (Co-S (int))	-32.6	+0.303												
Avg (Co-S (d))	-47.1	+0.473												
Avg (ALL)	-27.9	+0.306												

References

- (1) Sheberla, D.; Sun, L.; Blood-Forsythe, M. A.; Er, S.; Wade, C. R.; Brozek, C. K.; Aspuru-Guzik, A.; Dinca, M. High Electrical Conductivity in Ni₃(2,3,6,7,10,11-hexaiminotriphenylene)₂, a Semiconducting Metal-Organic Graphene Analogue. *J. Am. Chem. Soc.* **2014**, *136*, 8859–8862.
- (2) Zhao, B.; Zhang, J.; Feng, W.; Yao, Y.; Yang, Z. Quantum spin Hall and Z₂ metallic states in an organic material. *Phys. Rev. B: Condens. Matter Mater. Phys.* **2014**, *90*, 201403.
- (3) Foster, M. E.; Sohlberg, K.; Allendorf, M. D.; Talin, A. A. Unraveling the Semiconducting/Metallic Discrepancy in Ni₃(HITP)₂. *J. Phys. Chem. Lett.* **2018**, *9*, 481–486.
- (4) Foster, M. E.; Sohlberg, K.; Spataru, C. D.; Allendorf, M. D. Proposed Modification of the Graphene Analogue Ni₃(HITP)₂ To Yield a Semiconducting Material. *J. Phys. Chem. C* **2016**, *120*, 15001–15008.
- (5) Hmadeh, M. et al. New Porous Crystals of Extended Metal-Catecholates. *Chem. Mater.* **2012**, *24*, 3511–3513.
- (6) Genetic Algorithms in Search, O.; Machine Learning, ., Addison-Wesley
- (7) Wang, J.; Wolf, R. M.; Caldwell, J. W.; Kollman, P. A.; Case, D. A. Development and testing of a general amber force field. *J. Computat. Chem.* **2004**, *25*, 1157–1174.
- (8) Mardirossian, N.; Head-Gordon, M. B97M-V: A combinatorially optimized, range-separated hybrid, meta-GGA density functional with VV10 nonlocal correlation. *J. Chem. Phys.* **2016**, *144*, 214110.
- (9) Shao, Y. et al. Advances in molecular quantum chemistry contained in the Q-Chem 4 program package. *Mol. Phys.* **2015**, *113*, 184–215.

- (10) Breneman, C. M.; Wiberg, K. B. Determining atom-centered monopoles from molecular electrostatic potentials. The need for high sampling density in formamide conformational analysis. *J. Comput. Chem.* **1990**, *11*, 361–373.
- (11) Clough, A.; Skelton, J.; Downes, C.; de la Rosa, A.; Yoo, J.; Walsh, A.; Melot, B.; Marinescu, S. Metallic conductivity in a two-dimensional cobalt dithiolene metalorganic framework. *J. Am. Chem. Soc.* **2017**, *139*, 10863–10867.
- (12) Goedecker, S.; Teter, M.; Hutter, J. Separable dual-space Gaussian pseudopotentials. *Phys. Rev. B* **1996**, *54*, 1703–1710.
- (13) Zhao, Y.; Truhlar, D. G. A new local density functional for main-group thermochemistry, transition metal bonding, thermochemical kinetics, and noncovalent interactions. *J. Chem. Phys.* **2006**, *125*, 194101.
- (14) Zhao, Y.; Truhlar, D. G. Density Functionals with Broad Applicability in Chemistry. *Acc. Chem. Res.* **2008**, *41*, 157–167.
- (15) Weigend, F. Accurate Coulomb-fitting basis sets for H to Rn. *Phys. Chem. Chem. Phys.* **2006**, *8*, 1057–1065.
- (16) Weigend, F.; Ahlrichs, R. Balanced basis sets of split valence, triple zeta valence and quadruple zeta valence quality for H to Rn: Design and assessment of accuracy. *Phys. Chem. Chem. Phys.* **2005**, *7*, 3297–3305.
- (17) <https://www.basissetexchange.org>.
- (18) Cramer, C. J. E. o. C. C. T.; Models; 2nd ed.; John Wiley Sons: Chichester, .
- (19) Zhao, Y.; Truhlar, D. The M06 suite of density functionals for main group thermochemistry, thermochemical kinetics, noncovalent interactions, excited states, and transition elements: two new functionals and systematic testing of four M06-class functionals and 12 other functionals. *Theor. Chem. Acc.* **2008**, *120*, 215–241.

- (20) Frisch, M. J. et al. Gaussian 16 Revision A.03. Gaussian Inc. Wallingford CT 2016.
- (21) Smith, T., W.; Forester DL POLY 2.0: A general-purpose parallel molecular dynamics simulation package. *J. Mol. Graph.* **1996**, *14*, 136–141.
- (22) Tuckerman, M. E. Statistical mechanics: Theory and molecular simulation (Oxford University Press, 2010).
- (23) Leach, A. R. Molecular modeling: Principles and applications (Pearson Prentice Hall, 2001).
- (24) Barona, M.; Ahn, S.; Morris, W.; Hoover, W.; Notestein, J. M.; Farha, O. K.; Snurr, R. Q. Computational Predictions and Experimental Validation of Alkane Oxidative Dehydrogenation by Fe₂M MOF Nodes. *ACS Cat.* **2020**, *10*, 1460–1469.